



Synthesis of ultrathin mesoporous NiCo_2O_4 nanosheets on carbon fiber paper as integrated high-performance electrodes for supercapacitors

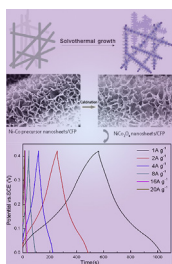
Fangze Deng, Lin Yu*, Gao Cheng, Ting Lin, Ming Sun, Fei Ye, Yongfeng Li

School of Chemical Engineering and Light Industry, Guangdong University of Technology, Guangzhou 510006, PR China

HIGHLIGHTS

- Ultrathin mesoporous NiCo_2O_4 nanosheets on carbon fiber paper were prepared by a facile method.
- The electrode possesses a high specific capacitance of 999 F g^{-1} at 20 A g^{-1} .
- The capacitance loss is 15.6% after 3000 cycles (discharged at 10 A g^{-1}).

GRAPHICAL ABSTRACT



ARTICLE INFO

Article history:

Received 5 October 2013

Received in revised form

4 November 2013

Accepted 19 November 2013

Available online 1 December 2013

Keywords:

Spinel nickel cobaltate

Ultrathin materials

Nanosheets

Carbon fiber paper

Supercapacitor

ABSTRACT

Two-dimensional ultrathin mesoporous NiCo_2O_4 nanosheets on carbon fiber paper (CFP) are synthesized through a facile solvothermal method combined with a post thermal treatment. The well interconnected ultrathin NiCo_2O_4 nanosheets directly grown on the carbon nanofibers could allow for easy diffusion of the electrolyte, shorten the transport path of ion and electron and accommodate the strain during cycling. As a result, superior pseudocapacitive performance is achieved with large specific capacitance of 999 F g^{-1} at a high current density of 20 A g^{-1} . The capacitance loss is 15.6% after 3000 cycles at a current density of 10 A g^{-1} , displaying good cycle ability and high rate capability.

© 2013 Elsevier B.V. All rights reserved.

1. Introduction

Supercapacitors, which can be classified into electrical double-layer (EDLC) and pseudocapacitors based on their underlying charge-storage mechanism, are promising power sources for many portable systems and hybrid electric vehicles because of their high power density, excellent pulse charge–discharge characteristics and long cycle life [1–4]. To date, the practical applications of

supercapacitors are still seriously hindered due to the unsatisfactory performance of the electrode materials, such as low specific capacitance of carbon based materials, poor cycling stability of transition metal oxides, and very high cost of RuO_2 based materials. Therefore, more efforts are still desired to further improve the electrochemical performance of electrode materials in order to build better supercapacitors with both high power and energy densities at a reasonable cost.

Up to now, numerous efforts have been made to investigate inexpensive pseudoactive transition-metal-based oxides or hydroxides, such as MnO_2 [5–7], NiO [8,9], Ni(OH)_2 [10–12], Co_3O_4 [13–18], CoO [19] and Co(OH)_2 [14,20,21], because these materials

* Corresponding author. Tel.: +86 20 39322202; fax: +86 20 39322231.

E-mail addresses: gych@gdut.edu.cn, zhoujunli19851111@163.com, hukis@126.com (L. Yu).

can produce much higher specific capacitances than typical carbon-based EDLCs and electronically conducting polymers. Among metal oxide materials, spinel NiCo_2O_4 holds great promise as a supercapacitors electrode material owing to its ultrahigh specific capacitance and rate capabilities that result from its greater electronic conductivity and electrochemical activity than single component nickel or cobalt oxides [22–25]. However, due to the short diffusion distance (~ 20 nm) of electrolytes into pseudocapacitor electrodes [26,27], only the surface part of electroactive materials can effectively contribute to the total capacitance, thus leading to a less satisfactory. To maximize the electrochemical performance of pseudocapacitors at high rates, it is critical to engineer the electrodes with large amount of electroactive sites and enhance the kinetics of ion and electron transport in electrodes and at the electrode–electrolyte interface. Based on the above considerations, considerable efforts have been dedicated to growing electroactive nanostructures on conductive substrates to be directly used as integrated electrodes for supercapacitors [28–31]. The integrated electrodes construction can avoid the “dead surface” in traditional slurry-derived electrode and allow for more efficient charge and mass exchange. Therefore, it will be of great significance to develop effective and facile methods to grow electroactive materials on conductive substrates for high energy density supercapacitors.

It has been well established that the morphology [32], crystallinity [12], porosity [33] of electrode materials play a key role in the high performance supercapacitors. Specially, as for the morphology, two-dimensional (2D) nanosheets can exhibit better cycling performance compared to one-dimensional (1D) nanorods or nanowires, and this is because that the 2D feature is favorable for efficient ion and electron transport and can better accommodate the structural change in the electrochemical reaction [14,32,34,35]. Several reports are available on the supercapacitor properties of 1D (such as nanowires [29,36], nanorods [24,32]) and 2D (such as nanosheets [22,28,32]) NiCo_2O_4 on 3D Ni foam. Although 3D nickel foam was widely used as the current collector, as the above reports adopted, owing to its huge supporting area and high electrical conductivity [37], however, experimental evidence assumes that using Ni foam can produce substantial errors to the specific capacitance values, especially when small amount of electrode active material is used in the measurement [38,39]. On the other hand, low-cost carbon fiber paper (CFP), a network of micro-sized carbon fibers with large surface area, high porosity and good electric conductivity, has been reported to be a promising current collector and backbone for conformal coating of transition metal oxides for supercapacitors [15,17,31,40]. Herein, we present our findings on the fabrication of ultrathin mesoporous 2D NiCo_2O_4 nanosheets on CFP with robust adhesion and application for supercapacitors electrodes. Remarkably, the as-prepared 3D CFP supported ultrathin mesoporous NiCo_2O_4 nanosheets hierarchical architectures dramatically enhanced redox kinetics at high charge/discharge rates while manifests high specific capacitance and good cycling stability at high rates, making it a promising electrode for supercapacitors.

2. Experimental

Synthesis of NiCo_2O_4 mesoporous nanosheets on CFP: All the chemicals were of analytical grade and were used without further purification. Commercial CFP (approximately $1\text{ cm} \times 4\text{ cm}$, from Shanghai hesen Electronic Co. Ltd.) were cleaned by ultrasonication in 5 M HCl aqueous solution, absolute ethanol and deionized water for 15 min each. 0.5 mmol of $\text{Co}(\text{NO}_3)_2 \cdot 6\text{H}_2\text{O}$, 0.25 mmol of $\text{Ni}(\text{NO}_3)_2 \cdot 6\text{H}_2\text{O}$, 1.5 mmol of hexamethylenetetramine were dissolved into 12 mL of absolute methanol by vigorous magnetic stirring to form a transparent pink solution. The solution was

transferred into a 25 mL Teflon-lined stainless steel autoclave. Then, a piece of the pre-treated CFP was put vertically in the above autoclave, heated to 180°C , and kept at that temperature for 12 h. After it was cooled down to room temperature, the product was ultrasonically cleaned for several times with DI water and ethanol, dried at 60°C for 2 h. Finally, the samples were annealed at 350°C in air for 3 h. The mass loading of the NiCo_2O_4 mesoporous nanosheets on CFP was around 0.8 mg cm^{-2} .

2.1. Materials characterization

The morphology of the samples was characterized by scanning electron microscopy (SEM, Hitachi, S-3400N) and transmission electron microscopy (TEM, JEOL, JEM-2100). The high-resolution TEM (HRTEM) images were recorded using a JEOL-2100 microscope. The crystal phase of the products was examined by X-ray diffraction (XRD, Bruker, D8-Advance, $\text{Cu K}\alpha$, $\lambda = 1.5406\text{ \AA}$). UV Laser Raman Spectroscopy (LabRAM HR800) was applied to study the chemical compositions and structures of the NiCo_2O_4 products. The nitrogen sorption measurements were performed using an ASAP 2020 instrument at 77 K.

2.2. Electrochemical measurements

Electrodes were tested on Autolab PGSTAT302N Electrochemical Workstation in a three-electrode electrochemical cell using a 2 M KOH aqueous solution as electrolyte at room temperature. The CFP supported electroactive materials ($\sim 1\text{ cm}^2$ in area) serves directly as the working electrode. The powder working electrode used for the comparison was prepared by mixing the active materials (80 wt %), acetylene black (10 wt %) and poly(tetrafluoroethylene) (PTFE, 10 wt %) to obtain a slurry. A small amount of absolute ethanol was then added to the mixture to promote homogeneity. After that, the mixture was coated onto the CFP ($1\text{ cm} \times 1\text{ cm}$) to form the electrode layer by drying at 120°C for 12 h. Pt foil and a saturated calomel electrode (SCE) were used as the counter electrode and the reference electrode, respectively. The specific capacitance is calculated according to the following equations:

$$C = \frac{1}{mv(V_c - V_a)} \int_{V_a}^{V_c} I(V) dV \quad (1)$$

$$C = \frac{I\Delta t}{m\Delta V} \quad (2)$$

where C (F g^{-1}) was specific capacitance, m is the mass of the electroactive materials in the electrodes (g), v is the potential scan rate (V s^{-1}), V_a is the anodic potential (V), V_c is the cathodic potential (V), I (V) is the response current density (A) and V is the potential (V). In equation (2), I (A) represented discharge current and m (g), ΔV (V), and Δt (s) designated mass of active materials, potential drop during discharge and total discharge time, respectively.

3. Results and discussion

3.1. Synthesis and characterization

The fabrication process of the NiCo_2O_4 nanosheets on CFP is shown in Fig. 1. The binary nickel–cobalt precursor can be produced on CFP by a precipitation reaction between Ni^{2+} , Co^{2+} and OH^- released from hexamethylenetetramine and methanol decomposition [15]. Then, the formed precursor was thermally transformed to black NiCo_2O_4 supported on the CFP by a simple

oxidation reaction. Thermogravimetric analysis of the as-grown precursor on the CFP and bare CFP was conducted in order to determine the calcination temperature and the typical results are shown in Fig. S1 (Supporting information). The gradual weight loss from room temperature to ca. 250 °C represents the evaporation of physically adsorbed water of the binary nickel–cobalt precursor. The obvious mass loss from 250 to 400 °C is attributed to the thermal decomposition of the precursor, which is expected to evolve extensive gases leading to the formation of pore within the resultant oxide. The TG results show that it is reasonable to set the annealing temperature at 350 °C.

Fig. 2 shows the XRD patterns of the NiCo_2O_4 supported on CFP and the NiCo_2O_4 powder scratched from CFP. As seen from Fig. 2a, besides the three typical strong peaks originating from the CFP substrate, other four relatively weak diffraction peaks are observed at 2θ values of 36.7°, 44.6°, 59.1° and 65.0°, which that can be indexed to (311), (400), (511) and (440) plane reflections of the spinel NiCo_2O_4 (JCPDF file no. 20–0781). Such result is quite in agreement with the NiCo_2O_4 power diffraction peak (Fig. 2b), manifesting that NiCo_2O_4 nanosheets have successfully grown on the CFP substrate.

Further, Raman spectroscopy was also used to characterize the phase composition and structure of the NiCo_2O_4 nanosheets. As seen in Supporting information Fig. S2, the peaks at 188, 456, 510, and 649 cm^{-1} correspond to F_{2g} , E_g , F_{2g} , and A_{1g} modes of the NiCo_2O_4 nanosheets, respectively [31]. Only the Co–O and Ni–O vibrations of NiCo_2O_4 are detected, indicating the Ni–Co precursor is completely decomposed after calcinating at 350 °C, which is consistent with the above TG analysis.

Fig. 3 shows a representative SEM image of the binary Ni–Co precursor and the NiCo_2O_4 supported on the CFP substrate. As can be seen from Fig. 3a–c, the Ni–Co precursor nanosheets are uniformly grown on the carbon nanofibers forming a large-scale conformal coating. From the enlarged views (Fig. 3b,c), the nanosheets are interconnected with each other to form a wall-like structure, which might possess better mechanical strength [28]. In addition, the nanosheets exhibit a hierarchical array feature with empty space among adjacent nanosheets. This feature could benefit the penetration of the electrolyte, which may contribute to the optimization of electrochemical performance [22]. After annealing at a relatively low temperature of 350 °C for 3 h with a slow heating rate of 1 °C min^{-1} , these Ni–Co precursor nanosheets can be easily converted to crystalline NiCo_2O_4 . Importantly, as shown in Fig. 3d–f, the well-interconnected ultrathin nanosheet morphology is perfectly retained after the annealing treatment, which could be

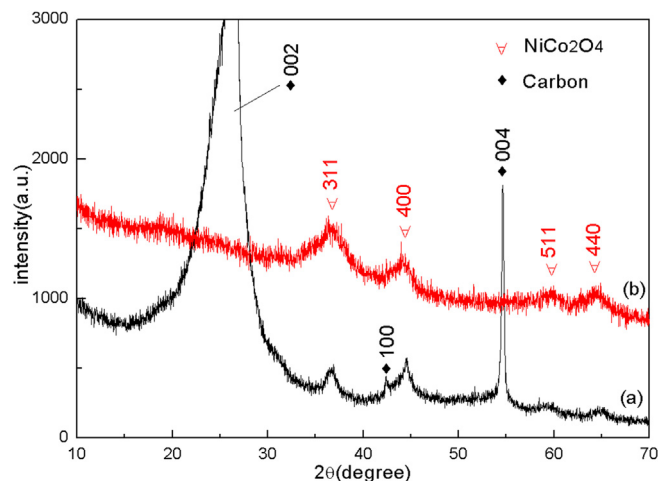


Fig. 2. XRD pattern of (a) the final ultrathin mesoporous NiCo_2O_4 nanosheets/CFP and (b) the NiCo_2O_4 nanosheets powder scratched from CFP.

derived from the robust support of carbon nanofibers and the slow heating rate applied during the annealing. These NiCo_2O_4 nanosheets are further characterized by TEM as shown in Fig. 4. The low-magnification image (Fig. 4a) indicates that the nanosheets are continuous with a smooth surface. Interestingly, a magnified view of the crystalline NiCo_2O_4 nanosheets (Fig. 4b,c) clearly indicates mesopores are uniformly distributed throughout the whole surface of nanosheets. The size of the mesopores is estimated to be in the range of 2–5 nm. It should be noted that the lattice spacings of NiCo_2O_4 could not be observed clearly, indicating that the NiCo_2O_4 phase was not good enough in crystallinity, in agreement with the result of XRD study (Fig. 2). The nitrogen adsorption and desorption isotherms of the NiCo_2O_4 nanosheets are shown in Fig. S3 (Supporting information), and the Brunauer–Emmett–Teller (BET) surface area is calculated to be as high as 206.7 $\text{m}^2 \text{g}^{-1}$. Distinct hysteresis loop can be observed in the range of 0.45–1.0 P/P_0 , which suggests the presence of a mesoporous structure of nanosheets. Our BET result obtained for the nanosheets in the present study is higher than that of reported values (Lou and Zhang 112.6 $\text{m}^2 \text{g}^{-1}$ [28]. Jiang et al. 202.2 $\text{m}^2 \text{g}^{-1}$ [25]. Hsu and Hu 123.9 $\text{m}^2 \text{g}^{-1}$ [41]). The high surface area is favorable for better supercapacitor performance of the composites. The pore size distribution of the sample calculated by desorption isotherm using

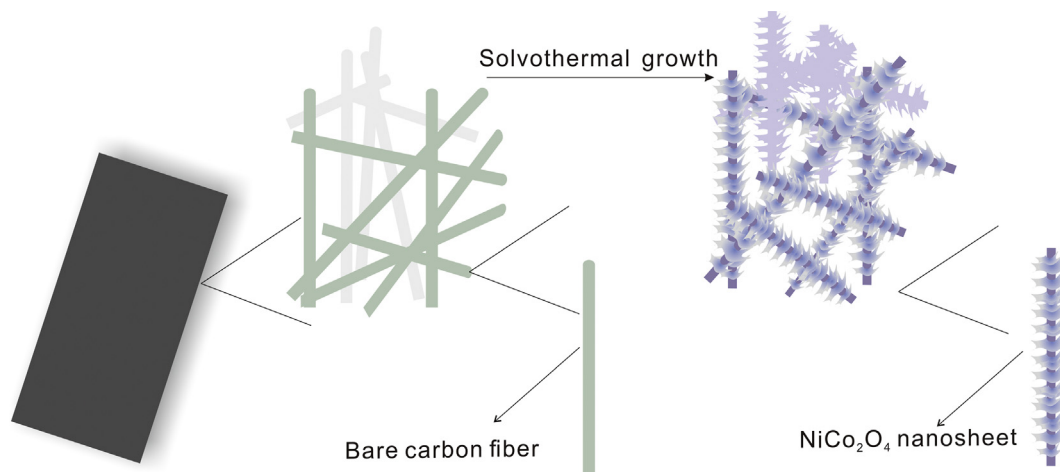


Fig. 1. Schematic illustration for the formation processes of the NiCo_2O_4 nanosheets on CFP.

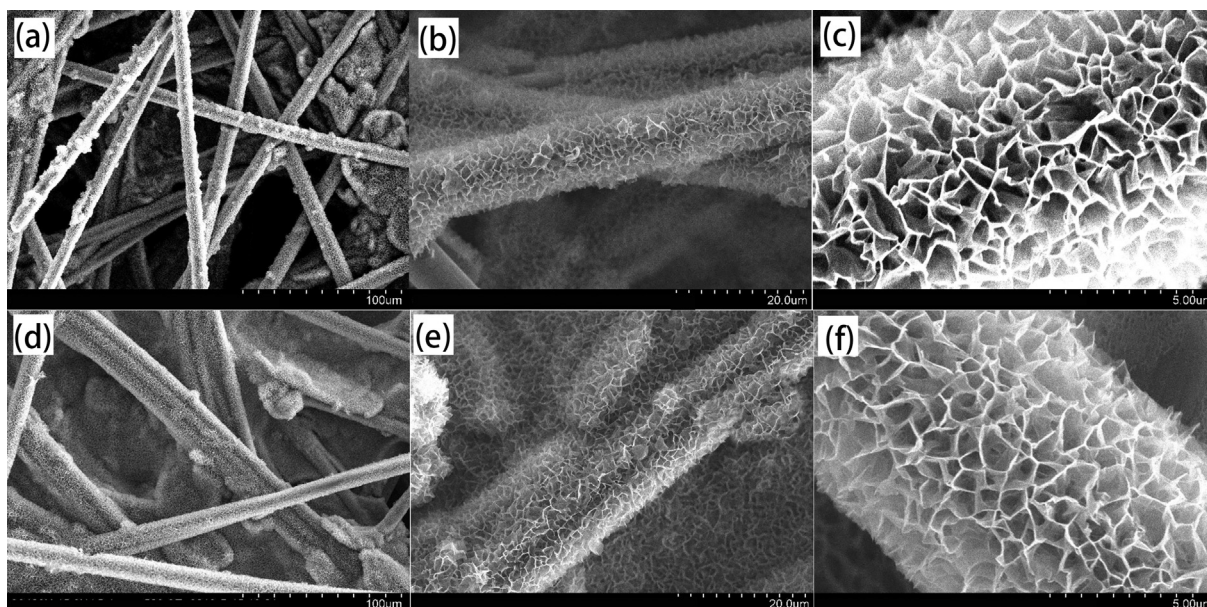


Fig. 3. Typical SEM images at different magnifications: (a–c) Ni–Co precursor nanosheets on CFP; (d–f) the final NiCo_2O_4 nanosheets on CFP after annealing at $350\text{ }^\circ\text{C}$ for 3 h in air with a heating rate of $1\text{ }^\circ\text{C min}^{-1}$.

Barret–Joyner–Halenda (BJH) method is also shown (the inset Fig. S3), indicating a pore size range of 2–5 nm, which is consistent with the above TEM observation. The formation of the mesopores could be related to the gas release during the decomposition of the Ni–Co precursor when using hexamethylenetetramine as the capping agent. Moreover, the corresponding selected-area electron diffraction (SAED) pattern (Fig. 4d) indicates the polycrystalline nature of these nanosheets. The three distinct diffraction rings can be readily indexed to the (311), (400) and (440) planes of the NiCo_2O_4 phase, which is consistent with the XRD result.

3.2. Electrochemical characterization

To evaluate the electrochemical performance of CFP supported NiCo_2O_4 nanosheet electrodes, we performed cyclic voltammetry (CV) measurements with various sweep rates ranging from 5 to 80 mV s^{-1} (Fig. 5a). The shape of the CV curves reveals the pseudocapacitive characteristics derived from Faradaic reactions. Clearly, a pair of well-defined redox peaks within -0.25 to 0.55 V (vs. SCE) is visible in all CV curves, and this pair of peaks is mainly attributed to the Faradaic redox reactions related to M–O/M–O–OH

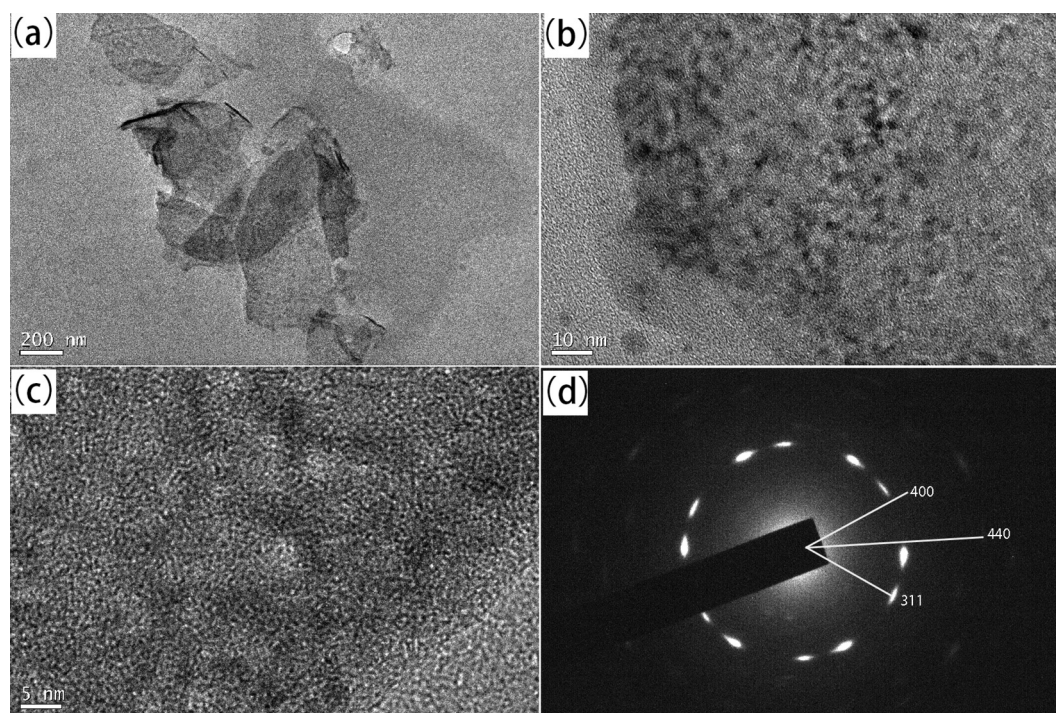


Fig. 4. TEM and HRTEM analysis of the NiCo_2O_4 nanosheets scratched from CFP: (a) morphology at a low magnification. (b,c) Observation of the mesoporous feature at high magnification. (d) SAED pattern of the ultrathin mesoporous NiCo_2O_4 nanosheets.

(M represents Ni or Co) [42]. The peaks are located at around 0.051 and 0.122 V when the scan rate is 5 mV s^{-1} . With the sweep rate rising from 5 to 80 mV s^{-1} , the position of the cathodic peak shifts from 0.051 to -0.041 V . This phenomenon indicates the hybrid electrode has low resistance, which is derived from the high electric conductivity of CFP backbone and the well contact between the electroactive NiCo_2O_4 nanosheets and the CFP substrate. Furthermore, a linear relation between the oxidation peak current at different scan rates and the square root of the scan rate is observed (Fig. S4, Supporting information), showing that the redox reaction is a diffusion-controlled process and reversible. The specific capacitance C (F g^{-1}) calculated from the area under the CV curve [10,12], are 1400, 1299, 1070, 820, 761 and 696 F g^{-1} at scan rates of 5, 10, 20, 40, 60 and 80 mV s^{-1} , respectively. With increasing scan rate, the specific capacitance decreases gradually (Fig. S5, Supporting information), which can be attributed to some active surface areas becoming inaccessible for charge storage with scan rate rise. It should be pointed out that the specific capacitance of the NiCo_2O_4 nanosheets electrodes decreases to 696 F g^{-1} at a very high scan rate of 80 mV s^{-1} , this result indicates the excellent capacitive behavior and high-rate capability of the NiCo_2O_4 /CFP electrodes.

Further, we characterized the charge–discharge behaviors of the ultrathin mesoporous NiCo_2O_4 nanosheets electrodes under galvanostatic conditions. As shown in Fig. 5b, the nearly symmetric potential–time curves at all current densities imply the high charge–discharge coulombic efficiency and low polarization of the unique electrode. This implied that the embedded carbon fiber network may enhance not only the conductivity of the composite electrode but also the charge transfer rate of the NiCo_2O_4 electrodes due probably to improved interface between NiCo_2O_4 and carbon

fiber during annealing. The calculated specific capacitance as a function of the discharge current density is plotted in Fig. 5c. Specially, the specific capacitance obtained is 1422, 1424, 1396, 1338, 1013 and 999 F g^{-1} at the discharge current densities of 1, 2, 4, 8, 16 and 20 A g^{-1} , respectively. The contribution of the carbon fiber paper to the capacitance is negligible (Fig. S6, Supporting information). Therefore, the total capacitance arises primarily from the redox pseudocapacitance of the loaded NiCo_2O_4 , demonstrating that the specific capacitance calculated from equation (1) is convincing. In addition, over the current density range, the specific capacitance decreases to 70% of its initial value, indicating that our synthesized NiCo_2O_4 /CFP composites have better rate performance compared to those reported results [32,42]. This might be attributed to the unique hierarchical network architecture, which can provide massive electroactive sites and facilitate transport of the electrolyte [11]. More importantly, the direct contact of every interconnected nanosheet with CFP substrate makes the composite materials possess better mechanical strength and shortens the diffusion paths of the ion and electron [18]. To further test these suggested advantages of the NiCo_2O_4 /CFP electrode, powder working electrode was fabricated on CFP for comparison with the same loading density of 0.8 mg cm^{-2} . The CV curves of the two types of electrodes are shown in Fig. S7 (Supporting information) at the scan rate of 5 mV s^{-1} , from which we can see that the CV curve area and discharge time of the NiCo_2O_4 /CFP electrode is much higher than that the powder electrode, indicating better capacitive performance of the integrated NiCo_2O_4 electrode.

The cycling stability of the NiCo_2O_4 /CFP electrode is also evaluated by the repeated charging–discharging measurement at a constant current density of 10 A g^{-1} as shown in Fig. 5d. When a

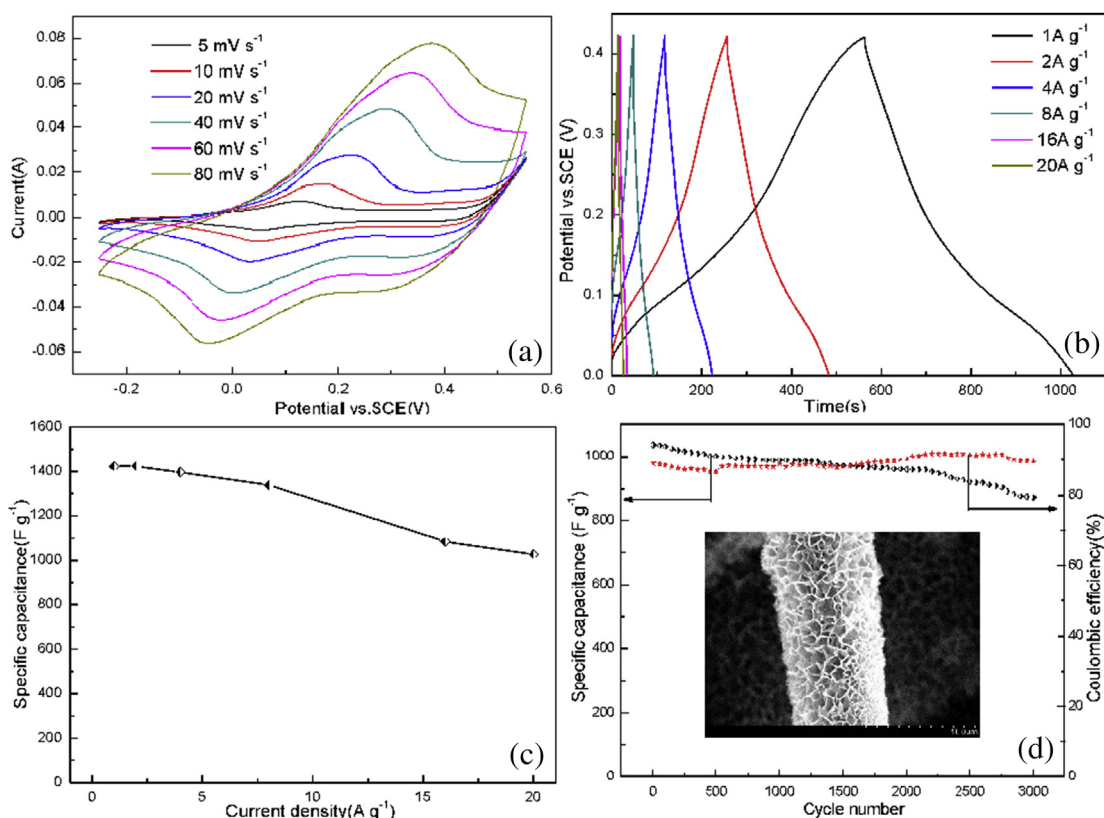


Fig. 5. Electrochemical characterizations of the CFP-supported NiCo_2O_4 nanosheet electrodes: (a) CV curves at various scan rates ranging from 5 to 80 mV s^{-1} . (b) Charge/discharge voltage profiles at various current densities ranging from 1 to 20 A g^{-1} . (c) The calculated capacitance as a function of current density according to the data in (b). (d) The capacitance and coulombic efficiency as a function of cycle number at a constant current density of 10 A g^{-1} (NiCo_2O_4 nanosheets after charging/discharging for 3000 cycles at a constant current density of 10 A g^{-1} in inset).

discharge current density of 10 A g^{-1} is applied, the specific capacitance is 1036 F g^{-1} in the first cycle, and it gradually decreases to 874 F g^{-1} over 3000 cycles, resulting in an overall capacitance loss of ca. 15.6%. The result is lower than that reported for mesoporous NiCo_2O_4 nanosheets grown on nickel foam [28], but higher than NiCo_2O_4 nanosheets grown on carbon fabric [43] tested under similar conditions. The inset figure in Fig. 5d shows the SEM image of the NiCo_2O_4 mesoporous nanosheets after charging–discharging for 3000 cycles at a current density of 10 A g^{-1} . As can be seen, the morphology and structure of the nanosheets are well-retained, except for the increased roughness on the nanosheet surface, caused by the high-rate redox reactions during the repeated charge–discharge processes. All in all, considering the relatively high discharge current density of 10 A g^{-1} (2–5 times that of commonly used value), the cycle ability is satisfying. Besides, coulombic efficiency stays around 90% over the total cycles, indicating a high charge–discharge reversibility of the as-prepared NiCo_2O_4 nanosheets/CFP electrodes.

4. Conclusions

In summary, we have prepared NiCo_2O_4 /CFP composite electrodes using a facile solvothermal method combined with a post annealing treatment. With this tailored architecture, the self-supported hybrid electrode showed high specific capacitance of 1422 and 999 F g^{-1} at current densities of 1 and 20 A g^{-1} , respectively, and desirable cycling stability and rate capability. The excellent performance is attributed to the high porosity and good electric conductivity of CFP substrate and the well interconnected ultrathin NiCo_2O_4 nanosheets. In view of the excellent electrochemical performance and the facile and cost-effective synthesis route, the NiCo_2O_4 /CFP hierarchical hybrid nanostructures might hold great promise as advanced electrode materials for high-performance supercapacitors.

Acknowledgments

This work was financially supported by the National Natural Science Foundation of China (21306026), Natural Science Foundation of Guangdong Province (10251009001000003, S2012010009680), the Scientific Program of Guangdong Province (2012A030600006) and the Fund of Higher Education of Guangdong Province (cgzhd1104).

Appendix A. Supporting information

Supplementary data related to this article can be found at <http://dx.doi.org/10.1016/j.jpowsour.2013.11.048>.

References

- [1] P. Simon, Y. Gogotsi, *Nat. Mater.* 7 (2008) 845–854.

- [2] J.R. Miller, P. Simon, *Science* 321 (2008) 651–652.
- [3] J. Jiang, Y. Li, J. Liu, X. Huang, C. Yuan, X.W. Lou, *Adv. Mater.* 24 (2012) 5166–5180.
- [4] W. Wei, X. Cui, W. Chen, D.G. Ivey, *Chem. Soc. Rev.* 40 (2011) 1697–1721.
- [5] X. Lang, A. Hirata, T. Fujita, M. Chen, *Nat. Nanotechnol.* 6 (2011) 232–236.
- [6] Q. Li, Z.-L. Wang, G.-R. Li, R. Guo, L.-X. Ding, Y.-X. Tong, *Nano Lett.* 12 (2012) 3803–3807.
- [7] R. Liu, S.B. Lee, *J. Am. Chem. Soc.* 130 (2008) 2942–2943.
- [8] G. Zhang, L. Yu, H.E. Hoster, X.W. Lou, *Nanoscale* 5 (2012) 877–881.
- [9] S. Vijayakumar, S. Nagamuthu, G. Muralidharan, *ACS Appl. Mater. Interface* 5 (2013) 2188–2196.
- [10] J. Yan, Z. Fan, W. Sun, G. Ning, T. Wei, Q. Zhang, R. Zhang, L. Zhi, F. Wei, *Adv. Funct. Mater.* 22 (2012) 2632–2641.
- [11] J. Ji, L.L. Zhang, H. Ji, Y. Li, X. Zhao, X. Bai, X. Fan, F. Zhang, R.S. Ruoff, *ACS Nano* 7 (2013) 6237–6243.
- [12] H.B. Li, M.H. Yu, F.X. Wang, P. Liu, Y. Liang, J. Xiao, C.X. Wang, Y.X. Tong, G.W. Yang, *Nat. Commun.* 4 (2013) 1894.
- [13] X. Xia, J. Tu, Y. Zhang, X. Wang, C. Gu, X.-b. Zhao, H.J. Fan, *ACS Nano* 6 (2012) 5531–5538.
- [14] X. Xia, J. Tu, Y. Zhang, J. Chen, X. Wang, C. Gu, C. Guan, J. Luo, H.J. Fan, *Chem. Mater.* 24 (2012) 3793–3799.
- [15] R.B. Rakhi, W. Chen, D. Cha, H.N. Alshareef, *Nano Lett.* 12 (2012) 2559–2567.
- [16] C. Yuan, L. Yang, L. Hou, L. Shen, X. Zhang, X.W. Lou, *Energy Environ. Sci.* 5 (2012) 7883–7887.
- [17] L. Yang, S. Cheng, Y. Ding, X. Zhu, Z.L. Wang, M. Liu, *Nano Lett.* 12 (2012) 321–325.
- [18] Y. Li, B. Tan, Y. Wu, *J. Am. Chem. Soc.* 128 (2006) 14258–14259.
- [19] C. Zhou, Y. Zhang, Y. Li, J. Liu, *Nano Lett.* 13 (2013) 2078–2085.
- [20] L. Wang, Z.H. Dong, Z.G. Wang, F.X. Zhang, J. Jin, *Adv. Funct. Mater.* 23 (2012) 2758–2764.
- [21] J. Jiang, J. Liu, R. Ding, J. Zhu, Y. Li, A. Hu, X. Li, X. Huang, *ACS Appl. Mater. Interface* 3 (2011) 99–103.
- [22] C. Yuan, J. Li, L. Hou, X. Zhang, L. Shen, X.W. Lou, *Adv. Funct. Mater.* 22 (2012) 4592–4597.
- [23] T.Y. Wei, C.H. Chen, H.C. Chien, S.Y. Lu, C.C. Hu, *Adv. Mater.* 22 (2010) 347–351.
- [24] G.Q. Zhang, H.B. Wu, H.E. Hoster, M.B. Chan-Park, X.W. Lou, *Energy Environ. Sci.* 5 (2012) 9453–9456.
- [25] H. Jiang, J. Ma, C. Li, *Chem. Commun.* 48 (2012) 4465–4467.
- [26] C.-C. Hu, K.-H. Chang, M.-C. Lin, Y.-T. Wu, *Nano Lett.* 6 (2006) 2690–2695.
- [27] Z. Lu, Q. Yang, W. Zhu, Z. Chang, J. Liu, X. Sun, D.G. Evans, X. Duan, *Nano Res.* 5 (2012) 369–378.
- [28] G. Zhang, X.W. Lou, *Adv. Mater.* 25 (2013) 976–979.
- [29] Q. Wang, X. Wang, B. Liu, G. Yu, X. Hou, D. Chen, G. Shen, *J. Mater. Chem. A* 1 (2013) 2468–2473.
- [30] X.Y. Liu, Y.Q. Zhang, X.H. Xia, S.J. Shi, Y. Lu, X.L. Wang, C.D. Gu, J.P. Tu, *J. Power Sources* 239 (2013) 157–163.
- [31] L. Huang, M. Liu, *Nano Lett.* 13 (2013) 3135–3139.
- [32] G. Zhang, X.W. Lou, *Sci. Rep.* 3 (2013) 1470.
- [33] S. Kondrat, C.R. Perez, V. Presser, Y. Gogotsi, A.A. Kornyshev, *Energy Environ. Sci.* 5 (2012) 6474–6479.
- [34] L. Hu, H. Zhong, X. Zheng, Y. Huang, P. Zhang, Q. Chen, *Sci. Rep.* 2 (2012) 986.
- [35] G. Wang, L. Zhang, J. Zhang, *Chem. Soc. Rev.* 41 (2012) 797–828.
- [36] L. Yu, G. Zhang, C. Yuan, X.W. Lou, *Chem. Commun.* 49 (2013) 137–139.
- [37] Z. Tang, C.-h. Tang, H. Gong, *Adv. Funct. Mater.* 22 (2012) 1272–1278.
- [38] W. Xing, S. Qiao, X. Wu, X. Gao, J. Zhou, S. Zhuo, S.B. Hartono, D. Hulicova-Jurcakova, *J. Power Sources* 196 (2011) 4123–4127.
- [39] M. Grdeń, M. Alsabet, G. Jerkiewicz, *ACS Appl. Mater. Interface* 4 (2012) 3012–3021.
- [40] Y. Luo, J. Jiang, W. Zhou, H. Yang, J. Luo, X. Qi, H. Zhang, D.Y.W. Yu, C.M. Li, T. Yu, *J. Mater. Chem.* 22 (2012) 8634–8640.
- [41] C.-T. Hsu, C.-C. Hu, *J. Power Sources* 242 (2013) 662–671.
- [42] H. Wang, Q. Gao, L. Jiang, *Small* 7 (2011) 2454–2459.
- [43] J. Du, G. Zhou, H. Zhang, C. Cheng, J. Ma, W. Wei, L. Chen, T. Wang, *ACS Appl. Mater. Interface* 5 (2013) 7405–7409.